Particle settling and vertical mixing in the Saharan Air Layer as seen from an integrated model, lidar, and in-situ perspective

Josef Gasteiger[1,2], Silke Groß[3], Daniel Sauer[3], Moritz Haarig[4], Albert Ansmann[4], and Bernadett Weinzierl[2]

[1]Meteorologisches Institut, Ludwig-Maximilians-Universität, München, Germany
[2]Faculty of Physics, University of Vienna, Vienna, Austria
[3]Institut für Physik der Atmosphäre, Deutsches Zentrum für Luft- und Raumfahrt, Oberpfaffenhofen, Germany
[4]Leibniz Institute for Tropospheric Research, Leipzig, Germany

Correspondence to: Josef Gasteiger (josef.gasteiger@univie.ac.at)

Abstract.

Long-range transport of aerosol in the Saharan Air Layer (SAL) across the Atlantic plays an important role for weather, climate, and ocean fertilization. However, processes occurring within the SAL and their effects on aerosol properties are still unclear. In this work we study particle settling and vertical mixing within the SAL based on measured and modeled vertical aerosol profiles in the upper 1 km of the transported SAL. We use ground-based lidar measurements and airborne particle counter measurements over the western Atlantic, collected during the SALTRACE campaign, as well as space-based CALIOP lidar measurements from Africa to the western Atlantic in the summer season. In our model we take account of the optical properties and the Stokes gravitational settling of irregularly-shaped Saharan dust particles.

We test two hypotheses about the occurrence of vertical mixing within the SAL over the Atlantic to explain the aerosol profiles observed by the lidars and the particle counter. Our first hypothesis (H1) assumes that no mixing occurs in the SAL leading to a settling-induced separation of particle sizes. The second hypothesis (H2) assumes that vertical mixing occurs in the SAL allowing large super-micron dust particles to stay airborne longer than without mixing.

The uncertainties of the particle linear depolarization ratio (δ_l) profiles measured by the ground-based lidars are comparable to the modeled differences between H1 and H2 and do not allow us to conclude which hypothesis fits better. The SALTRACE in-situ data on particle number concentrations show a presence of large particles near the SAL top that is inconsistent with H1. Also the analysis of the CALIOP measurements reveals that the average δ_l profile over the western Atlantic is inconsistent with H1. Furthermore, it was found that the average δ_l profile in the upper 1 km of the SAL does not change along its transport path over the Atlantic. These findings give evidence that vertical mixing within the SAL is a common phenomenon with significant consequences for the evolution of the size distribution of the super-micron dust particles during transport over the Atlantic. Further research is needed to precisely characterize the processes that are relevant for this phenomenon.

1 Introduction

The Saharan Air Layer (SAL) carries large amounts of Saharan aerosol particles towards the western Atlantic Ocean and the Americas, in particular during summer time (e.g., Prospero and Carlson, 1972; Carlson and Prospero, 1972; Schütz, 1980; Tsamalis et al., 2013). The SAL over the African continent often is a well-mixed convective layer from the hot surface to about
5 4-6 km above sea level (Ben-Ami et al., 2009; Knippertz et al., 2009; Cuesta et al., 2009; Esselborn et al., 2009). As soon as the SAL reaches the Atlantic, it is lifted over a comparatively cold marine boundary layer. As a consequence, the radiative heating at the bottom of the SAL, which is a strong driving force for convection, vanishes. However, vertical mixing within the SAL over the Atlantic might be possible due to other radiative or dynamic effects. Knowledge about those processes is quite limited but they can be important for the evolution of the particle size distribution during transport. Changes in size distribution
10 can have significant effects for radiative properties and deposition of Saharan aerosols (e.g., Otto et al., 2009; Mahowald et al., 2014).

Size distribution measurements performed at Izaña (Canary Islands) and Puerto Rico (Caribbean) by Maring et al. (2003) revealed that Saharan dust particles with $r > 3.6$ μm are preferentially removed during the transport over the Atlantic. Maring et al. (2003) cannot explain their measurements by assuming that Stokes gravitational settling is the only process occurring
15 during transport over the Atlantic. They have to reduce the Stokes settling velocity by 0.0033 m s^{-1} to match the measurements, which could be an indication for vertical mixing of air during the transport. Also the lack of significant vertical changes of particle size distributions found by Reid et al. (2003) in the Caribbean indicates that settling is counteracted by some other processes.

Lidar remote sensing is a powerful tool to localize and characterize aerosols, including their size distributions. The particle
20 linear depolarization ratio δ_l (Sassen, 1991), measured by advanced lidar systems, is a particularly useful parameter to characterize Saharan aerosols. For example, Liu et al. (2008) characterize in a case study a dust outbreak that was transported from the Sahara over the Atlantic. They use measurements of the CALIOP lidar (Winker et al., 2009), which is operated on-board the CALIPSO satellite and measures δ_l at a wavelength of 532 nm. Liu et al. (2013) investigate Asian dust and its transport over the Pacific using data from the same instrument. The network EARLINET (Pappalardo et al., 2014) provides a comprehensive data
25 set on ground-based lidar measurements throughout Europe, which is useful to study Saharan aerosols transported to Europe (see e.g., Mattis et al., 2002; Papayannis et al., 2008; Wiegner et al., 2011). During field campaigns like PRIDE (Reid et al., 2003), SAMUM (Heintzenberg, 2009; Ansmann et al., 2011), Fennec (Ryder et al., 2013), and SALTRACE (Weinzierl et al., 2017), Saharan aerosol has been measured using a wide set of techniques, including lidar, photometer, and airborne in-situ instrumentation. The combination of different measurement techniques enables one to better constrain the properties of the
30 rather complex Saharan aerosol. Polarization-sensitive (near-)backscattering by dusty aerosols is studied also in laboratories (e.g., Sakai et al., 2010; Järvinen et al., 2016).

Yang et al. (2013) investigate Saharan aerosols on their way over the Atlantic based on δ_l data from CALIOP. They use δ_l from volumes that the CALIPSO operational algorithm classified as dust-laden and average δ_l, as function of height above sea level, over the summer season 2007. The averaged δ_l profiles show an increasing height dependence with increasing distance

from Africa. Over the western Atlantic they find the largest δ_l values at altitudes of about 4-5 km and a decrease of δ_l with decreasing altitude. Yang et al. (2013) explain the averaged CALIOP δ_l profiles with settling-induced separation of particle shapes using a model which assumes that particles with nearly spherical shape settle faster and have smaller δ_l than particles with stronger deviation from spherical shape.

5   In our study we investigate the Saharan aerosol transport over the Atlantic by combining advanced modeling efforts with data obtained from ground-based lidar, from airborne particle counters, and from the CALIOP lidar. We show theoretical profiles for Saharan aerosols considering gravitational settling as function of particle size and shape, and two hypotheses about the occurrence of vertical mixing within the SAL. The lidar-relevant optical properties are simulated based on the particle microphysics explicitly using an optical model. We compare our modeled profiles with the measured data that we evaluate as

10   function of distance from the SAL top. The ground-based and airborne measurements used in our study were performed during the SALTRACE field campaign (Weinzierl et al., 2017) in the summer 2013 in the vicinity of Barbados (Caribbean). From CALIOP, we use night-time profile data covering 15 summer months and the Saharan aerosol transport region from Africa to the Caribbean.

After describing our modeling approach (Sect. 2) we investigate modeled lidar profiles after five days of transport without

15   vertical mixing (Sect. 3.1), which is a typical transport time of Saharan aerosol to the Caribbean. The sensitivity of δ_l profiles to particle shape (Sect. 3.2) and to the shape dependence of the settling velocity (Sect. 3.3) is investigated subsequently. In Sect. 3.4 we model the effect of day-time convective vertical mixing occurring in the SAL during transport. Subsequently, the modeled profiles are compared in a case study to lidar and in-situ profiles measured in Barbados during SALTRACE (Sect. 4) to test our two hypotheses about vertical mixing in the SAL over the Atlantic. In Sect. 5 we continue testing these hypotheses

20   by using averaged CALIOP profiles, before we give concluding remarks in Sect. 6.

2   Model description

Our model describes Saharan aerosols in the SAL. We consider six irregular dust particle shapes, as introduced by Gasteiger et al. (2011), with shapes A-C being deformed prolate spheroids with varying aspect ratio, shape D an aggregate, and shapes E-F edged particles with varying aspect ratio (these shapes are depicted further down in Fig. 5 together with their aspect

25   ratios). Though this low number of model shapes is not sufficient to represent all aspects of Saharan dust in full detail, model ensembles composed of these dust shapes and small water-soluble particles can be used to approximate optical properties of Saharan aerosols (Gasteiger et al., 2011). We assume the particles to be randomly oriented. We furthermore assume that the SAL initially is well-mixed and that gravitational settling of the aerosol particles is the only process when no vertical mixing occurs. We also consider the case of a diurnal cycle of the convective vertical mixing activity.

3

2.1 Stokes settling

The settling velocity v of a particle relative to the ambient air is determined by the balance between gravitation force F_g and drag force F_d if other forces can be neglected. The gravitation force is given by

$$F_g = \frac{4}{3}\pi r_v^{\,3} \rho g \tag{1}$$

with the volume-equivalent radius r_v of the particle, the gravitational acceleration $g = 9.81$ m s^{-2}, and the particle density ρ that we assume to be $2.6 \cdot 10^3$ kg m^{-3} for mineral dust particles (Hess et al., 1998). The drag force of a settling aerosol particle in the size range from $r \approx 0.5$ µm to $r \approx 10$ µm (being in the Stokes' drag regime) can be approximated by

$$F_d = 6\pi \eta r_c v \tag{2}$$

with the dynamic viscosity of air $\eta = 17$ µPa s (approx. value for a temperature of 0°C and tropospheric pressures) and the cross-section-equivalent radius r_c of the particle. We use r_c instead of r_v in this equation because the drag force is related more to the cross section of the particle than to its volume.

We note that using r_c in Eq. 2 is an approximation because determining the exact Stokes drag force of an irregularly-shaped particle is a more complex issue, see e.g. Loth (2008). The drag force of a particle larger than $r \approx 10$ µm is stronger than calculated with Eq. 2. For example in case of spherical particles, F_d is increased by about 5 % for $r = 20$ µm and about 15 % for $r = 30$ µm compared to Stokes law (Hinds, 1999). In addition, because of the flow around the settling particle, coarse non-spherical particles can become horizontally aligned. Using the formula about the probability distributions of orientation angles of prolate spheroids compiled by Ulanowski et al. (2007), we estimate that settling-induced alignment occurs for dust particles with $r > 5$ µm. In the Stokes regime, for typical dust aspect ratios of 1.6-1.8, F_d of a spheroid in horizontal orientation is on average about 5 % stronger than the average F_d of the same particle in random orientation (Clift et al., 1978). In the following, we stick to Eq. 2 for the calculation of F_d because these deviations have only negligible effect on the profiles presented below.

Setting $F_g = F_d$ and using the conversion factor $\xi_{vc} = r_v / r_c$ (Gasteiger et al., 2011) results in a settling velocity of the particle relative to the ambient air of

$$v = \frac{2g\rho}{9\eta} \cdot r_c^2 \cdot \xi_{vc}^3 \tag{3}$$

ξ_{vc} of our six irregular model shapes are 0.955 (shape A), 0.932 (B), 0.911 (C), 0.871 (D), 0.925 (E), and 0.866 (F). Note that the dynamic shape factor χ (Hinds, 1999) is $\chi = \xi_{vc}^{-1}$ if r_v is assumed, and $\chi = \xi_{vc}^{-3}$ if r_c is assumed for the radius. Henceforth unless otherwise stated, we use the cross-section-equivalent radius $r = r_c$ for describing particle size.

As a result of gravitational settling during a time period t_s without vertical mixing, the maximum particle radius r_{max} at a distance dz from the upper boundary of the SAL is given by

$$r_{max} = \sqrt{\frac{9\eta dz}{2g\rho \xi_{vc}^3 t_s}} \tag{4}$$

Fig. 1 illustrates r_{max} as function of dz for different settling time periods t_s. The solid lines show r_{max} for a conversion factor $\xi_{vc} = 0.9$, which is in the range of our dust model shapes. The vertical axis was chosen such that the top of the SAL ($dz = 0$
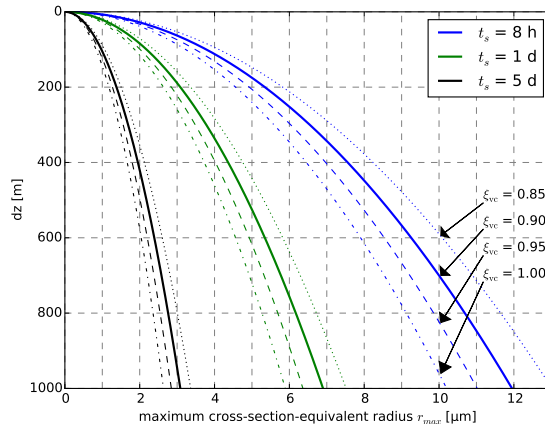
Figure 1. Maximum cross-section-equivalent radius r_{max} of dust particles as function of distance dz from the SAL top after different settling time periods t_s assuming different shape-dependent conversion factors ξ_{vc}. $\xi_{\mathrm{vc}} = 1$ corresponds to spherical particles.

m) is at the top of the figure. For example, at $t_s = 5$ d, no particles with radii $r > 2$ μm and $\xi_{\mathrm{vc}} = 0.9$ exist in the upper 400 m of the SAL.

2.2 Hypotheses about occurrence of vertical mixing

In our first hypothesis (H1) we assume that no vertical mixing of air occurs in the SAL over the Atlantic. By contrast, in our
5   second hypothesis (H2) we assume a diurnal cycle of the convection activity. The idea behind H2 is that the SAL is heated by absorption of sunlight by the aerosol particles triggering convective vertical mixing during the day. In nature the physics behind vertical mixing of SAL air might differ from what we assume in our idealized model H2 (see discussion). The possibility of vertical mixing in the SAL is consistent with the almost height-independent potential temperature profiles observed within the SAL (see e.g. Carlson and Prospero (1972) or further down on Fig. 8). We emphasize that the convection activity studied here
10   is not connected to the convection occurring in the marine boundary layer (which sometimes affects the lower parts of the SAL).

Both hypotheses are illustrated in Fig. 2. We model the transport for one vertical column, ignoring possible wind shear or convergence. For simplicity, we assume that the SAL reaches the Atlantic at first sunset. Furthermore, we assume convective vertical mixing always to be perfect though in reality convection may be weak and the vertical mixing imperfect. In case of
15   H2, the initial aerosol size distribution at $t_s = 0$ varies from night to night because a certain fraction of particles is removed by settling during the convection-free time each night before convective vertical mixing starts again with sunrise. The fraction f of particles that remains in the SAL after one night is calculated for $z_{\mathrm{settled}}(r, \xi_{\mathrm{vc}}) < H_{\mathrm{SAL}}$ using

$$f(r, \xi_{\mathrm{vc}}) = \frac{exp\left(\frac{H_{\mathrm{SAL}} - z_{\mathrm{settled}}(r, \xi_{\mathrm{vc}})}{H_{\mathrm{scale}}}\right) - 1}{exp\left(\frac{H_{\mathrm{SAL}}}{H_{\mathrm{scale}}}\right) - 1} \tag{5}$$
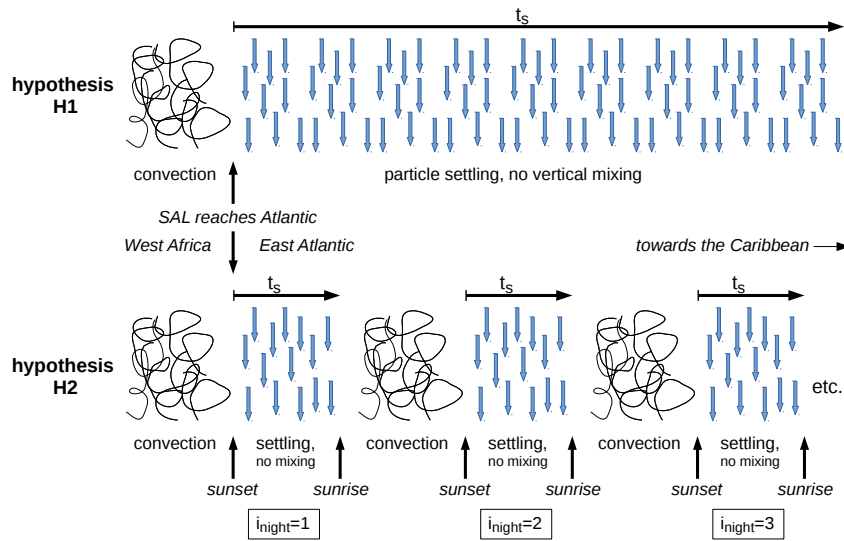
Figure 2. Schematic view of timing in hypotheses about the occurrence of settling and convective vertical mixing within the SAL.

where $z_{\mathrm{settled}}(r, \xi_{\mathrm{vc}})$ is the distance the particles have settled during the night. No particles with $z_{\mathrm{settled}}(r, \xi_{\mathrm{vc}}) > H_{\mathrm{SAL}}$ are in the SAL after the first night. z_{settled} is calculated using v from Eq. 3 and a night duration of 11 h, which is a typical value for the northern tropical Atlantic during summertime. H_{SAL} is the depth of the SAL within which convective vertical mixing occurs each day. We use $H_{\mathrm{SAL}} = 3$ km. In Eq. 5 we assume that the particles are well-mixed within the SAL at sunset. Those

5   particles that settle during the night below the lower boundary of the SAL (determined by H_{SAL}) are considered as removed from the SAL at sunrise when mixing starts again. Eq. 5 considers the exponential decrease of the air density, and thus the amount of aerosol (in case of well-mixed layers) with height. We assume a scale height $H_{\mathrm{scale}} = 10$ km, which implies an exponential decrease by a factor of e from the ground to 10 km height. This value of H_{scale} was estimated from the tropical standard atmosphere provided by Anderson et al. (1986).

10   Figure 3 shows for H2 the fraction of the particles present in the SAL at the beginning of each night (counted by i_{night} as illustrated in Fig. 2). This fraction is calculated from Eq. 5 using

$$f(r, \xi_{\mathrm{vc}})^{(i_{\mathrm{night}} - 1)} \tag{6}$$

and is multiplied with the initial aerosol size distribution, which is described below, to get the size distribution at the beginning of each night.

15   Henceforward in this paper, we denote the hypotheses and points of time using the following notation: For the first hypothesis we write [H1, t_s] and for the second hypothesis we write [H2, i_{night}, t_s].
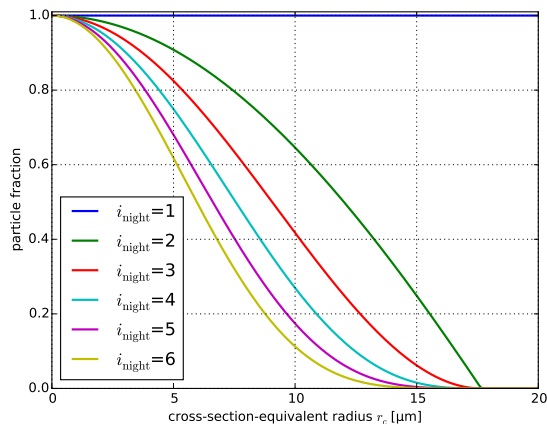
Figure 3. Fraction of particles (relative to initial size distribution) existing in SAL at beginning of each night ($t_s = 0$) in case of H2 and $\xi_{\mathrm{vc}} = 0.90$.

2.3 Aerosol mixtures and optical modeling

We simulate the optical properties of Saharan aerosols based on their microphysical properties (size, shape, refractive index) as described by Gasteiger et al. (2011) and use the reference ensemble described in that contribution as the initial aerosol ensemble at [H1, 0 h] and [H2, 1, 0 h]. The lidar-related optical properties of this ensemble are consistent with measurements

5 of Saharan aerosols over Africa (Gasteiger et al., 2011). The aerosol ensembles consist of four log-normal size modes with one mode of small water-soluble (WASO) particles and three modes of mineral dust particles, as defined for the desert mixture in OPAC (Koepke et al., 2015). For WASO particles, spherical shape, a relative humidity of 50 %, and a density of $\rho = 1.42 \cdot 10^3$ kg m^{-3} is assumed. Mixing of mineral dust with WASO particles is consistent with results presented by Kaaden et al. (2009) who found that Saharan aerosol particles in the smaller size ranges ($r < 0.1$-0.25 µm) consist mainly of ammonium sulfate.

10 Volatile ammonium sulfate particles were identified also in airborne in-situ measurements during SAMUM (Weinzierl et al., 2009) and SALTRACE (Weinzierl et al., 2017).

The mineral dust particles of the reference ensemble are an equiprobable mix of shapes B, C, D, and F (Gasteiger et al., 2011). The optical properties of dust particles with $2\pi r_v / \lambda \leq 25$ were calculated with the discrete dipole approximation code ADDA (Yurkin and Hoekstra, 2011) and for larger particles it was assumed that the lidar ratio S and the linear depolarization

15 ratio δ_l are size-independent, i.e. S and δ_l calculated for $2\pi r_v / \lambda = 25$ was applied also for larger particles.

It has been shown for Saharan aerosols that the refractive index varies from dust particle to dust particle (e.g., Kandler et al., 2011), and that this variability can have significant effects on lidar-relevant optical properties (Gasteiger et al., 2011). In our model, we consider the refractive index variability by the following approximating approach: The imaginary part of the dust refractive index, which is relevant for absorption, is distributed such that 50 % of the dust particles are non-absorbing while the

7

other 50 % have an imaginary part that is doubled compared to the value provided by OPAC, leading to good agreement with SAMUM lidar measurements (Gasteiger et al., 2011).

We apply a maximum cut-off radius r_{max} that is varied as function of distance dz from the SAL top as given by Eq. 4. The maximum r_{max} is 40 µm (at $dz \leq 1$ km only relevant for $t_s < 1$ h). In case of a diurnal cycle of convective vertical mixing (H2), we consider in addition the partial removal of particles due to settling each night, as described above (Eq. 6, Fig. 3). The evolution of the mineral dust size distribution for H2 (each night at $t_s = 0$) is illustrated in the supplement S-1.

We simulate vertical profiles of the extinction coefficient α, the backscatter coefficient β, the lidar ratio

$$S = \frac{\alpha}{\beta} = \frac{4\pi}{\omega_0 F_{11}(180°)} \tag{7}$$

and the linear depolarization ratio

$$\delta_l = \frac{1 - F_{22}(180°)/F_{11}(180°)}{1 + F_{22}(180°)/F_{11}(180°)} \tag{8}$$

Here, ω_0 is the single scattering albedo of the aerosol particles, $F_{11}(180°)$ and $F_{22}(180°)$ are elements of their scattering matrix at backward direction. We consider the height dependence of the particle concentration of the initially well-mixed layer by multiplying all modeled α and β profiles with $\exp(dz/H_{\mathrm{scale}})$. In this paper, α, β, S, and δ_l are always aerosol particle properties, i.e. without gas contributions.

3   Modeled lidar profiles

In this section we first present modeling results for our first hypothesis (H1) with a settling duration of $t_s = 5$ d, which is the typical time span for transport of aerosol in the SAL from the African coast to Barbados (e.g., Schütz, 1980). H1 is selected here because the effects are stronger than in case of H2. We investigate the sensitivity of the δ_l profile to the particle shape and the shape dependence of the settling velocity v. Finally in the last part of this section, we investigate the effect of the diurnal convective vertical mixing cycle (H2) on the δ_l profile.

3.1   Effect of particle settling (H1)

Vertical profiles of lidar-relevant optical properties of the aerosol in the upper 1 km of the SAL, modeled according to H1 after five days without vertical mixing of air ([H1, 5 d]), are shown in Fig. 4. The solid lines show results for the reference ensemble at three different lidar wavelengths (indicated by color). To illustrate the effect of the WASO particles, we also consider a case in which we removed all WASO particles (dashed lines of same colors).

The lidar ratio S increases towards the top of the SAL (Fig. 4a). S at $\lambda = 532$ nm and 1064 nm has peaks of about 75-80 sr in the upper 70 m of the SAL, decreasing again on the last few meters below the SAL top. Removing the WASO particles from the ensemble has a significant effect on S only near the top of the SAL (compare dashed with solid line).

We find a decrease of the linear depolarization ratio δ_l with decreasing distance dz from the SAL top (Fig. 4b). The absolute decrease of δ_l depends on wavelength; for example, from $dz = 1000$ m to $dz = 100$ m δ_l decreases by 0.065, 0.074, and 0.121
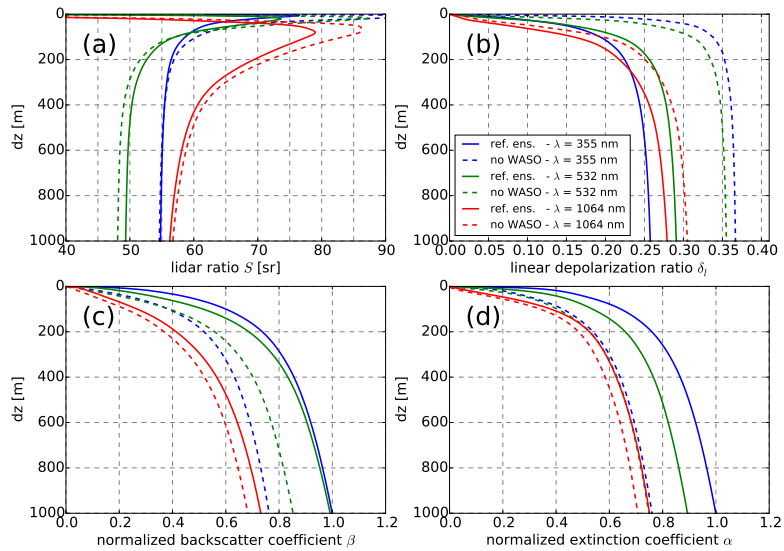
Figure 4. Optical aerosol properties of the upper 1 km of the SAL for [H1, 5 d] assuming the reference ensemble (solid lines) at three lidar wavelengths (indicated by color). β and α are normalized to the value of the reference ensemble at $\lambda = 355$ nm and $dz = 1000$ m. The dashed lines present profiles when WASO particles are removed from the reference ensemble.

at $\lambda = 355$ nm, 532 nm, and 1064 nm, respectively. Removing WASO particles strongly increases δ_l at all heights, in particular at short wavelengths (compare blue lines for $\lambda = 355$ nm), illustrating their importance in modeling δ_l of Saharan aerosols. The decrease of δ_l is shifted towards smaller dz if WASO is neglected but the general shape of the δ_l profiles does not change.

The backscatter coefficient β, normalized by β at $\lambda = 355$ nm and $dz = 1000$ m, is shown in Fig. 4c. It decreases with
5   decreasing dz; e.g. at $dz = 100$ m and the three lidar wavelengths, β of the reference ensemble is reduced by 41 %, 49 %, and 63 %, respectively, compared to β at $dz = 1000$ m.

The extinction coefficient α (Fig. 4d) also decreases towards the SAL top; the relative decrease, however, is smaller than for β, e.g. for the reference ensemble we find values of 36 %, 40 %, and 50 % for the height levels mentioned above. WASO particles influence the wavelength dependence of β and α at any dz.
10   In the following we focus on δ_l at $\lambda = 532$ nm because δ_l is the intensive aerosol property, i.e. not depending on the amount of particles, which can be measured with high vertical resolution (compared to S from Raman lidar) and many depolarization lidar systems operate at this wavelength.

3.2 Sensitivity of δ_l profiles to particle shape

The shape mixture in our reference ensemble may not be fully representative for desert aerosol. Therefore, it is worthwhile to
15   estimate the sensitivity of the lidar profiles to particle shape. Fig. 5 shows δ_l profiles at $\lambda = 532$ nm for [H1, 5 d] where all dust
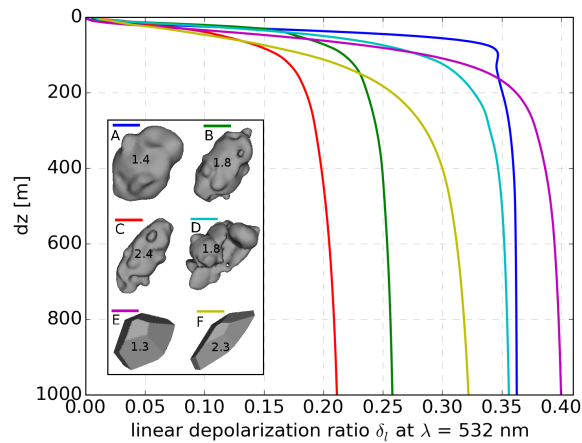
Figure 5. Linear depolarization ratio profiles at $\lambda = 532$ nm in the upper 1 km of the SAL for [H1, 5 d]. The reference ensemble is applied (as in Fig. 4), but only a single dust particle shape is assumed in each profile as indicated in the legend. The approx. aspect ratio is written on each particle.

particles of the reference ensemble were replaced by particles of only a single shape, as indicated in the legend together with their approx. aspect ratios. The other microphysical properties of the dust particles and the properties of the spherical WASO particles were left unchanged. For each profile, the shape-specific ξ_{vc}, as given above, is considered in the calculations.

The absolute value of δ_l at $\lambda = 532$ nm depends on particle shape with a variation range from about 0.2 to 0.4 at $dz = 1000$ m. δ_l of elongated shapes (C, F) tends to be smaller than δ_l of the more compact counterparts (A, E), illustrating that there is no direct correlation between large aspect ratios and large δ_l (in contrast to what is often assumed in the literature, e.g. Yang et al. (2013)). δ_l decreases with decreasing dz for all considered shapes and the decrease is not strongly sensitive to the selection of the particle shape. However, the decrease of δ_l in case of shapes D-F (aggregate particles, edged particles) tends to be shifted to larger dz compared to δ_l in case of shapes A-C (deformed spheroids). The sensitivity of δ_l profiles to realistic changes of the refractive index and the size distribution was found to be lower (not shown) than the sensitivity to the particle shape (Fig. 5).

3.3 Sensitivity of δ_l profiles to shape dependence of settling velocity

Yang et al. (2013) suggest a model for settling-induced separation of particle shapes to explain the observed height dependence of δ_l. They consider the shape dependence of the settling velocity v but not the size dependence of v. Here, we investigate how sensitive δ_l profiles are to the shape dependence of v compared to the size dependence of v. For this purpose, Fig. 6 shows δ_l profiles at $\lambda = 532$ nm for [H1, 5 d] and for three different shape mixtures, which are indicated by color (mixture BCDF corresponds to the reference ensemble used in most other parts of this paper). The solid lines illustrate results when shape-dependent ξ_{vc} are considered. By contrast, results shown as dashed lines assumed the average ξ_{vc} value (as displayed in the legend) for the settling of all dust shapes, implying that the shape dependence of v is switched off. For comparison also
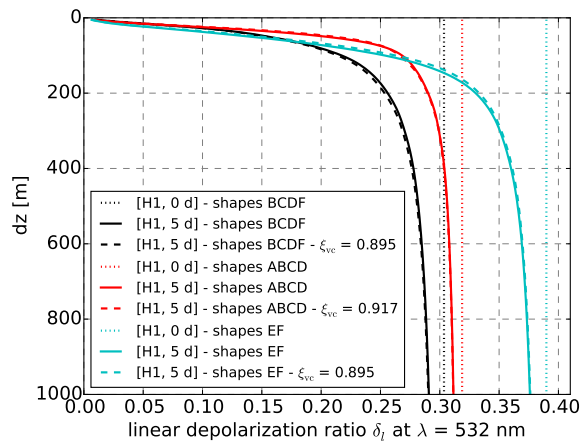
Figure 6. Analogous to Fig. 5, but assuming mixtures of different shapes of mineral dust particles as indicated in the legend (shapes BCDF = reference ensemble). The solid lines show profiles for [H1, 5 d]. The dashed lines show the same profiles when no shape dependence of the settling velocity is assumed (ξ_{vc} of all shapes is set to the average value, which is given in the legend). The dotted lines show the modeled profile at the beginning of the settling.

the initial δ_l profiles at [H1, 0 d] are shown as dotted lines. Thus, the differences between the dotted and the solid lines show the total settling effect after 5 days without vertical mixing and the differences between solid and dashed lines show the effect of the shape dependence of the settling velocity. The latter effect is much smaller than the total settling effect, independent of the assumed shape mixture. This allows us to conclude that the settling-induced separation of particle shapes is only of

5   minor importance for δ_l compared to the settling-induced separation of particle sizes. These results are consistent with results presented by Ginoux (2003).

3.4   Effect of diurnal convection cycle (H2)

Figure 7 shows δ_l profiles for both hypotheses, different time periods without mixing (t_s), and different number of nights (i_{night}), assuming our reference ensemble as the initial ensemble. The effect of settling on the δ_l profile increases with increas-

10   ing t_s, in particular in the upper few hundred meters of the SAL (H1, compare dashed lines). In case day-time vertical mixing occurs (H2), the night-time δ_l profile (shown here for 8 hours after sunset) changes only slightly from day to day, with the maximum changes occurring at lower altitudes (compare solid lines). For example, δ_l is reduced by about 0.007 at $dz = 1000$ m from the first night ($i_{night} = 1$) to the sixth night ($i_{night} = 6$). The differences between the δ_l profiles for H1 and those for H2 increase with time (lines of same color correspond to approx. the same transport time), illustrating the sensitivity of the δ_l

15   profiles to the occurrence of vertical mixing.

11
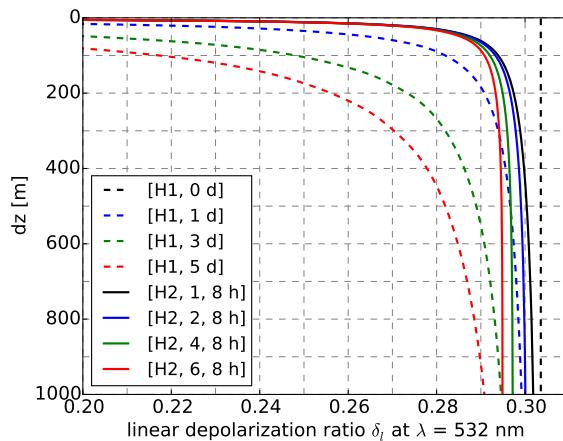
Figure 7. Linear depolarization ratio δ_l profiles at $\lambda = 532$ nm in the upper 1 km of the SAL for both hypotheses after different transport time periods.

4 Comparison with SALTRACE data

We now discuss our modeling results based on a comparison with aerosol data measured during the SALTRACE field campaign (Weinzierl et al., 2017) in the upper 1 km of the SAL and test our two hypotheses using this data set.

4.1 Lidar measurements

5   Lidar measurements and radiosonde launches were performed on the grounds of the Caribbean Institute for Meteorology and Hydrology in Bridgetown, Barbados (13.15° N, 59.62° W, 110 m above sea level). Data from the lidar system POLIS of the LMU (Munich) (Groß et al., 2015; Freudenthaler et al., 2016), data from the lidar system BERTHA of the TROPOS (Leipzig) (Althausen et al., 2000; Haarig et al., 2016), and radiosonde data measured by TROPOS are available. POLIS and BERTHA are Raman lidar systems, thus requiring strong temporal and vertical smoothing for the determination of profiles of lidar ratio

10   S and extinction coefficient α. A vertical smoothing length of at least 500 m is required for those properties, but even with this smoothing length the signal-to-noise ratio of the Raman measurements is still too low for a meaningful comparison with our modeled vertical profiles. Therefore, we restrict our comparison to the linear depolarization ratio δ_l and the backscatter coefficient β, for which a significantly shorter smoothing length is sufficient. Furthermore, we consider only $\lambda = 532$ nm for our comparison.

15   The lidar measurements presented in this section were performed around 0 UTC in the night from 10 to 11 July 2013. Sunset was at 22:28 UTC. Back trajectory analysis for this air mass using HYSPLIT (Draxler and Rolph, 2015) suggests that it had left the African continent about 5 days before the measurements (see supplement S-2). To test our hypotheses about the occurrence of vertical mixing, we assume for this comparison $t_s = 5$ d in case of H1, and $t_s = 2$ h and $i_{\text{night}} = 6$ in case of H2.

12
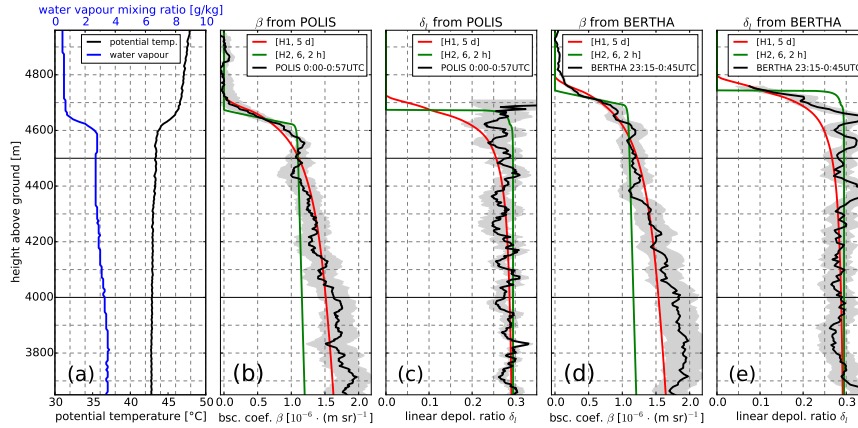
Figure 8. Vertical profiles over Barbados around 0 UTC on 11 July 2013. (a) Profile of potential temperature (black) and water vapour mixing ratio (blue) from a radiosonde launched at 23:39 UTC on 10 July 2013. (b) Particle backscatter coefficient β and (c) particle linear depolarization ratio δ_l at $\lambda = 532$ nm from POLIS measured between 0:00 UTC and 0:57 UTC on 11 July 2013. (d) Particle backscatter coefficient β and (e) particle linear depolarization ratio δ_l at $\lambda = 532$ nm from BERTHA measured between 23:15 UTC on 10 July 2013 and 0:45 UTC on 11 July 2013. The shaded area indicate the sum of the systematical and statistical uncertainties of the measured profiles. Corresponding modeled lidar profiles for H1 (red) and H2 (green) are shown. The SAL top heights of the modeled profiles were fitted to the measured β profiles (heights given in main text). A flat smoothing window of about 50 m is used for the measured and modeled lidar profiles.

Fig. 8a shows radiosonde data of water vapour mixing ratio (blue) and potential temperature (black). The potential temperature is nearly constant within the SAL, which extends up to about 4600 m above ground. This potential temperature profile indicates that vertical mixing might have occurred during the transport of this air mass over the Atlantic. The relative humidity at 4500 - 4600 m is about 50 % to 54 %. The vertical structure of the water vapour mixing ratio and the potential temperature
5   might be regarded as typical for the Saharan Air Layer (Carlson and Prospero, 1972).

Fig. 8b and Fig. 8c show β and δ_l profiles measured by POLIS (black line), temporally averaged over almost 1 hour, including the sum of the systematic and statistical uncertainties. Fig. 8d and Fig. 8e show β and δ_l profiles measured by BERTHA (black line), temporally averaged over 1.5 hours, including the estimated uncertainties. For comparison, also profiles modeled for our hypotheses H1 (red) and H2 (green) are plotted in Fig. 8. The SAL top heights of the modeled profiles were fitted to the
10   measured β profiles. The fitted SAL top height is 4700 m for H1 and 4650 m for H2 in case of POLIS, whereas it is 4770 m for H1 and 4720 m for H2 in case of BERTHA. Measured and modeled lidar profiles shown in Fig. 8 were vertically smoothed with a flat window of about 50 m length.

The measured β profiles are better fitted by the profile modeled for H1 than by the profile modeled for H2 (Fig. 8b and Fig. 8d). The modeled δ_l for H1 and H2 is generally close to the measured δ_l in the lower part of the SAL (Fig. 8c and 8e). At
15   the top of the SAL, where the measurement uncertainties are considerable, the measured δ_l profiles deviate from each other and no conclusion on whether H1 or H2 better explains the δ_l profiles can be drawn. At other days during SALTRACE, the lidar

13
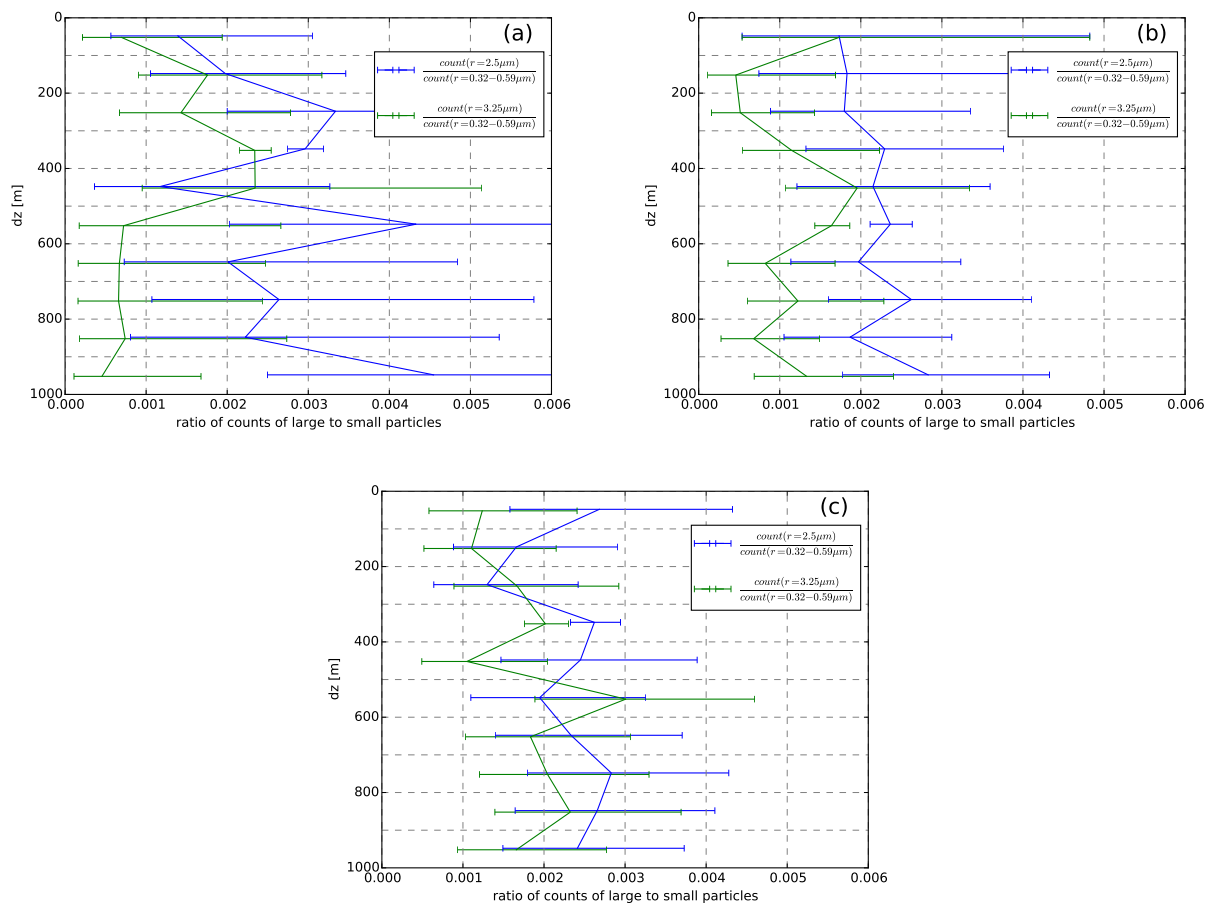
Figure 9. Ratios between counts in different size ranges measured by CAS-DPOL during aircraft ascent and descent (a) between 18:09 and 20:10 UTC on 22 June 2013, (b) between 15:14 and 16:42 UTC on 10 July 2013, and (c) between 12:45 and 13:50 UTC on 11 July 2013. The aircraft locations are illustrated in Fig. S-3 (supplement). The vertical axis shows the distance from the SAL top. The data was grouped in 100 m wide vertical bins. The error-bars are Poisson 95 % confidence intervals.

profiles and their uncertainties exhibit similar characteristics in the SAL (not shown). Our comparisons indicate that further reductions of uncertainties are desirable to identify transport effects within the SAL by means of lidar data. The investigation of profiles at other wavelengths, e.g. δ_l at $\lambda = 1064$ nm (Haarig et al., 2016), might also bring further insights.

4.2 Optical particle counter measurements

5 During SALTRACE, the Cloud and Aerosol Spectrometer with Depolarization Detection (CAS-DPOL manufactured by DMT, Boulder, CO, USA) was operated under a wing of the DLR research aircraft Falcon. The ambient air streams through this optical particle counter. It uses a laser as light source operating at $\lambda = 658$ nm and measures the intensity of light scattered

forward into 4°-12° by individual particles flying through its sampling area. Each particle is counted and from the measured intensity its size is inverted. The counts are collected in 30 size bins, covering a nominal radius range from 0.25 µm to 25 µm. These size bins and the size calibration used here were provided by the manufacturer of the instrument. The size-resolved in-situ data from CAS-DPOL allows us to test more directly the maximum cut-off radius calculated in case of H1.

5　　For this test we use data from flights performed during day-time on 22 June 2013, 10 July 2013, and 11 July 2013. The aircraft position at the time when the data used here was measured is illustrated in Fig. S-3 (supplement). To extract the information about settling-induced separation of sizes, we use size bins for which we would expect no counts at low dz due to settling in case of H1 and normalize them by counts measured with the same instrument in a size range that is almost not affected by settling (Fig. 1). The results are illustrated in Fig. 9. The blue lines show the counts in the nominal size bin r =

10　2.5 µm (size bin no. 17), whereas the green lines show the counts in the nominal size bin r = 3.25 µm (size bin no. 18), both normalized by the counts in the size bins from r = 0.32 µm to 0.59 µm (size bin no. 2-9). Analysis of calibration measurements performed during SALTRACE suggests that the sizes presented here are underestimated because the instrument optics was polluted by dust particles which reduced the amount of light reaching the detector.

　　The in-situ data is available at one second resolution, which corresponds to about 8 m vertical resolution during ascent and

15　descent of the investigated flights. Because of the low number of counts per second for coarse particles, we grouped the data in 100 m wide vertical bins. The vertical bins are described by their distance dz from the SAL top as determined from the CAS-DPOL data. The SAL top was at 3700 m asl both during ascent and descent on 22 June, at 5050 m during ascent and at 4900 m during descent on 10 July, and at 4630 m asl during ascent and at 4550 m asl during descent on 11 July 2013. Each dz bin covers about 25 seconds of data, except bins in which the ascent or descent was paused flying at constant altitude.

20　　As illustrated in Fig. 1, we expect in case of our first hypothesis (H1) that particles with $r \approx 2.5$ µm and larger are removed from $dz < 550$ m after 5 days over the Atlantic. However, the curves in Fig. 9 show that such particles are detected also in the upper 100 m of the SAL near Barbados. This indicates H1 to be unrealistic even if intrinsic uncertainties of the size determination by CAS-DPOL on the order of ±50 % are assumed. A similar height dependence was found also during the PRIDE campaign which was based on Puerto Rico (Reid et al., 2003). This suggests that some processes within the SAL keep

25　large particles longer in the air than expected from gravitational settling.

5　Comparison with average δ_l profiles from CALIOP

After presenting SALTRACE case studies in the previous section, we now use averaged CALIOP δ_l profiles to get a more general view on the modification of the aerosols during the transport over the Atlantic and to test our hypotheses. We note that in reality the SAL transport is much more complex than our hypotheses assume and varies from case to case. Nonetheless, we

30　expect that averaged profiles of the intensive property δ_l contains evidence about whether the occurrence of vertical mixing within the SAL is typical or not. In the following, we first describe how we calculate the average δ_l from the CALIOP data, then compare our modeling results to the averaged profiles in the upper 1 km of the SAL, and finally discuss our findings.

5.1 Averaging CALIOP data

We restrict our analysis to δ_l at 532 nm because this parameter is relatively insensitive to errors encountered in the extinction-backscatter retrieval (Liu et al., 2013), which may result, e.g. from uncertainties in the lidar ratio (Wandinger et al., 2010; Amiridis et al., 2013). We again analyze the upper 1 km of the SAL, where potential settling and mixing effects should be observable with lidar (Fig. 7). We use CALIPSO level 2 aerosol profile products v3.01 (NASA, 2010) of backscatter coefficients β and the perpendicular components of the backscatter coefficients $\beta_\perp$ at $\lambda = 532$ nm measured during summer 2007-2011, i.e. from June to August of each of the five years. We excluded profiles measured on 23 June 2009 and on 2 Aug 2009 because of unrealistic outliers found in the data from these days. Powell et al. (2009) describe how backscattering quantities are calculated from the CALIOP raw data. Vaughan et al. (2009) show the automated procedure to detect aerosol and cloud layers using these backscattering quantities, and Liu et al. (2009) demonstrate how aerosols are discriminated from clouds. We restrict our evaluation to measurements in the region from 10°N to 30°N and 0°W to 75°W. We group these measurements in three longitude ranges of 25° width along the transport path from Africa to the western Atlantic. Only night-time measurements are considered; all measurements were performed approximately 8 h after sunset.

The CALIOP measurements are performed with a vertical resolution of 30 m and a horizontal resolution of 330 m. The backscatter coefficients β and $\beta_\perp$ are provided in the level 2 data with a vertical resolution of 60 m (i.e. for bins of 60 m height) and a horizontal resolution of 5 km, which reduces the noise compared to the measured resolution. As discussed by Vaughan et al. (2009), aerosol features are detected with 30 m vertical resolution using an iterative procedure starting with the horizontal resolution of 5 km. As the noise can be considerable at 5 km resolution, in particular if particle concentrations are low, the horizontal resolution is subsequently increased to 20 km and 80 km to detect also weaker features. Depending on the results of the feature detection, the backscatter coefficients are horizontally averaged over 5 km, 20 km, or 80 km, and the horizontal averaging range can depend on height. In the following we use only data horizontally averaged over 5 km.

From the large set of aerosol profiles, the profiles that fulfill the following criteria are selected for averaging:

- Uppermost aerosol-containing bin between 3 and 8 km above sea level

- Both sub-bins (30 m height each) of uppermost aerosol-containing bin classified as aerosol-containing

- All 16 bins (i.e. up to $\approx$1 km) below uppermost aerosol-containing bin also classified as aerosol-containing

- No cloud-containing bin detected in or above 17 uppermost aerosol-containing bins

- Data horizontally averaged over 5 km (not 20 or 80 km) in each of the 17 uppermost aerosol-containing bins

- Linear depolarization ratio δ_l, averaged over 17 uppermost aerosol-containing bins, larger than 0.10

β and $\beta_\perp$ of each of the 17 vertical bins is summed up over all selected profiles. From these sums, the average δ_l for each bin is calculated according to

$$\delta_l = \frac{\sum \beta_\perp}{\sum \beta - \sum \beta_\perp}. \tag{9}$$
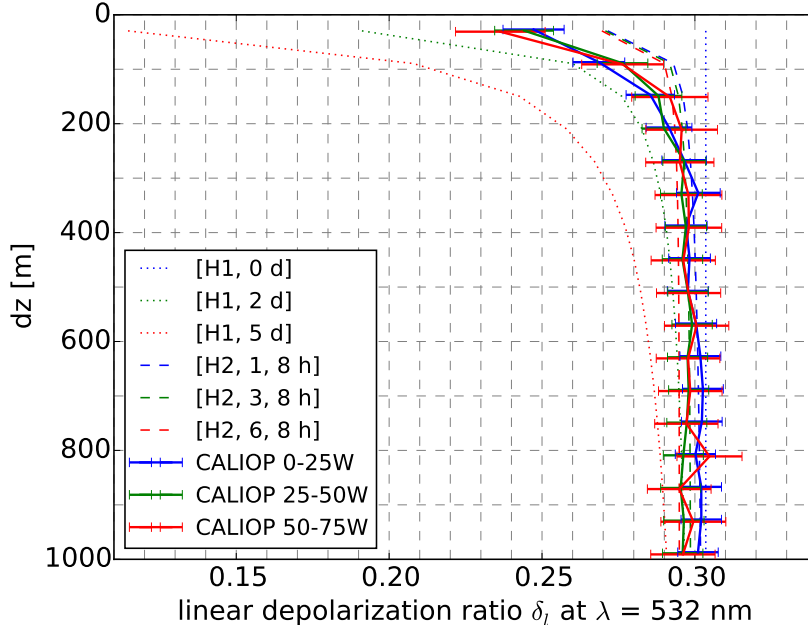
Figure 10. Linear depolarization ratio δ_l profiles at $\lambda = 532$ nm in the upper 1 km of the SAL. CALIOP profiles averaged over profiles from summer months 2007-2011 that fulfill conditions listed in the text are shown as blue, green, and red solid lines. The colors denote different longitude ranges. Error bars of the CALIOP profiles show the estimated statistical uncertainty $\Delta \delta_l$ of the average δ_l. For comparison also model results for both hypotheses are shown as dotted (H1) and dashed (H2) lines.

The measurement uncertainties $\Delta \beta$ and $\Delta \beta_{\perp}$ provided in the CALIOP profile data are based on a simplified analysis assuming that all the uncertainties are random, uncorrelated and produce no biases (Young, 2010). The magnitude of the uncertainties is mainly determined by the signal-to-noise ratio (Hunt et al., 2009). To calculate the estimated statistical uncertainty $\Delta \delta_l$ of the average δ_l value for each bin (Eq. 9), we sum up the squares of the measurement uncertainties of each profile and use

$$5 \quad \Delta \delta_l = \frac{\sqrt{\left(\sum \beta\right)^2 \cdot \sum \left(\Delta \beta_{\perp}\right)^2 + \left(\sum \beta_{\perp}\right)^2 \cdot \sum \left(\Delta \beta\right)^2}}{\left(\sum \beta - \sum \beta_{\perp}\right)^2}. \tag{10}$$

As we average over a large number of profiles, the uncertainties of the averaged profiles are reduced considerably compared to the uncertainties of single profiles.

5.2 Comparison with averaged profiles

Figure 10 shows the averaged δ_l profiles calculated from the CALIOP profile data considering all profiles that fulfilled the
10 above-mentioned criteria. The averaged data of the uppermost bin is plotted at $dz \approx 30$ m, the subsequent bin at $dz \approx 90$ m, etc. While the blue solid line shows the average δ_l close to the aerosol source region, the distance from the source region increases with the green line (central Atlantic) and red line (western Atlantic). A map illustrating these regions is provided in

the supplement S-4. Averages were taken over 9061, 9114, and 3846 individual profiles in the 3 respective regions along the SAL transport path. Considering the statistical uncertainty of the average, the average δ_l does not vary along the SAL transport path and is height-independent with values close to 0.30 for $dz > 250$ m. δ_l decreases towards the SAL top to values of about 0.23-0.25 in the uppermost bin.

5   Comparing the measured with the modeled profiles, it becomes clear that the strong decrease of δ_l in the upper 100 m of the SAL, as modeled for long-range transport without vertical mixing (H1, red dotted line), is not found in the averaged CALIOP data over the western Atlantic (red solid line). This indicates our first hypothesis (H1) to be unrealistic. A further result that renders H1 unlikely is the fact that the average δ_l profile from CALIOP is not modified during transport while one would expect significant changes of the δ_l profile during transport if H1 is assumed (compare the dotted lines of different colors).

10   The dashed lines in Fig. 10 show the δ_l profile when day-time convective vertical mixing is assumed (H2). These modeled δ_l profiles are relatively height-independent, except in the upper 100 m of the SAL. Fig. 10 shows that considering vertical mixing (using H2 instead of H1) reduces considerably the deviation of the model from the measurements after long range transport. Also the invariability of the average δ_l profile between the different regions is much better captured if H2 is assumed. Our model for H2 predicts a reduction of δ_l by about 0.007 at $dz = 1$ km after about 5 days (see dashed lines). This reduction is

15 not seen in the CALIOP profiles, possibly because it is within the range of the statistical uncertainty of the averaged δ_l profiles from CALIOP.

5.3   Discussion of comparison with averaged profiles

Our model assuming day-time vertical mixing (H2) explains the averaged CALIOP data and its invariability between the regions for the most part. However, deviations of the δ_l profile between this model and the averaged CALIOP data occur in

20 the upper 2-3 bins (compare dashed to solid lines in Fig. 10). The measurements indicate on average a stronger removal of large particles in the upper 100 m of the SAL over Africa and over the Atlantic than H2 suggests. We again emphasize that we average over a large number of different cases. The δ_l profiles may vary from case to case, which however is hard to quantify from the CALIOP data because of large statistical uncertainties of single profiles.

One source of deviation could be our settling and vertical mixing model in H2. We assume perfect mixing of particles over

25 the complete SAL when convection occurs and we assume a sharp boundary between the SAL and the layer above. But it might be plausible that some mixing occurs between the SAL and the layer above on the order of 10 m to 100 m. Thus, some Saharan aerosol near the upper boundary of the SAL might become decoupled from the mixing within the SAL, allowing there a stronger removal of large particles than H2 predicts. However, one fact that contradicts these considerations is that the measured δ_l profile seems to be independent of region while one would expect that such effects become larger with distance

30 from the source regions.

Another source of uncertainty is related to our aerosol model. Natural desert aerosol has very complex microphysical properties (e.g. Kandler et al., 2011), and as a consequence, our model of the Saharan aerosol mixtures contains several assumptions and the calculated optical properties are connected with uncertainties. Though we argue that our model mixture represents lidar-relevant optical properties of Saharan aerosols well (Gasteiger et al., 2011), we can not exclude that the deviations of

the modeled δ_l profiles (H2) from the averaged measurements in the upper 2-3 bins are related to assumptions in our aerosol mixture and the optical modeling approach.

A further aspect that needs to be kept in mind is that multiple scattering could affect the CALIOP measurements (Wandinger et al., 2010). In case of our SAL top study, the multiple scattering effect would increase with increasing dz as the lidar pulse penetrates the SAL from its top. It is well-known that with increasing amount of particles the multiple scattering effect increases (e.g. Bissonnette et al., 1995). Using the CALIOP profile data we do not find a significant dependence of the δ_l profiles on the absolute values of β (not shown), indicating that multiple scattering does not significantly affect the averaged δ_l profiles.

To investigate the CALIOP profiles in more detail, an analysis is provided in the supplement S-4, considering also 20 km and 80 km horizontal averages, the year-by-year variability, sub-bin classification, the cloud-aerosol discrimination, and the sensitivity to the δ_l threshold. The sensitivity of the averaged δ_l profile to these parameters was found to be low. As a consequence, it seems likely that the simplifications in H2 (including the optical model) are the reason for the remaining deviations near the SAL top. Also the average β profile (see supplement S-4), as well as the variability of the backscatter coefficient β from case to case (not shown), can not be explained using H2, showing the need to consider in future research further aspects for precise SAL transport modeling.

6 Summary and conclusions

Transport of aerosol in the Saharan Air Layer (SAL) over the Atlantic is relevant for weather and climate but important processes within the SAL still are not well understood. To gain insights in relevant processes, we developed a model which describes the modification of the vertical aerosol distribution in the upper 1 km of the SAL during transport based on the physical processes of gravitational settling and vertical mixing. From the vertical aerosol distributions, lidar profiles are calculated using explicit optical modeling. Sensitivity studies revealed (a) that generally the particle linear depolarization ratio decreases towards the SAL top for all considered model shapes, and (b) that the size dependence of the settling velocity is significantly more important for the linear depolarization ratio profile than the shape dependence of the settling velocity.

The model results were compared to lidar and in-situ measurements and two hypotheses about the occurrence of vertical mixing within the SAL were tested (H1 without mixing, H2 with mixing during the day). Comparisons with ground-based depolarization lidar measurements in Barbados, performed in the frame of the SALTRACE campaign, revealed that the measurement uncertainties are in the same order as the differences between both hypotheses. Vertically resolved in-situ measurements of the size distribution during SALTRACE found large particles in the upper part of the SAL that are not consistent with H1, indicating that vertical mixing occurs in the SAL over the Atlantic. These findings are supported by results from an analysis using night-time data from CALIOP. The CALIOP data shows that the average linear depolarization ratio profile in the upper 1 km of the SAL does not change along its transport path over the Atlantic, which disproves H1. These findings are consistent with results from other studies which found that long-range range transported Saharan aerosol contains unexpectedly large particles or that the aerosol properties do not change significantly during long-range transport, e.g. Reid et al. (2003); Maring

et al. (2003); Weinzierl et al. (2011); Mahowald et al. (2014); Denjean et al. (2016a, b); van der Does et al. (2016); Weinzierl et al. (2017).

We could show that vertical mixing occurs within the SAL and our model assuming day-time vertical mixing (H2), which is driven by the idea that the Saharan aerosol absorbs sunlight triggering convection, explains most data quite well. However, there are limitations of this idealized model. For example, profiles of extensive properties like the backscatter coefficient often can not be explained with H2 and remaining deviations from the averaged CALIOP depolarization data are still unexplained. We did not consider the possibility of weak vertical mixing, of size-selective particle removal at the lower boundary of the SAL during vertical mixing, or effects due to electrical fields in the SAL. Radiative effects in the thermal infrared might be an important aspect to consider for understanding the vertical mixing in the SAL, as discussed by Carlson and Prospero (1972). The development of turbulence due to vertical wind shear, more realistic air layer dynamics, and feedbacks of radiative effects with the dynamics (Chen et al., 2010) are possible further aspects to be considered for a precise understanding of the processes within the SAL, their variability, and their effect on size distributions and lifetime of super-micron particles.

References

Althausen, D., Müller, D., Ansmann, A., Wandinger, U., Hube, H., Clauder, E., and Zörner, S.: Scanning 6-Wavelength 11-Channel Aerosol Lidar, J. Atmos. Oceanic Technol., 17, 1469–1482, doi:10.1175/1520-0426(2000)017<1469:SWCAL>2.0.CO;2, 2000.

Amiridis, V., Wandinger, U., Marinou, E., Giannakaki, E., Tsekeri, A., Basart, S., Kazadzis, S., Gkikas, A., Taylor, M., Baldasano, J., and Ansmann, A.: Optimizing CALIPSO Saharan dust retrievals, Atmos. Chem. Phys., 13, 12 089–12 106, doi:10.5194/acp-13-12089-2013, 2013.

Anderson, G. P., Clough, S. A., Kneizys, F. X., Chetwynd, J. H., and Shettle, E. P.: AFGL atmospheric constituent profiles (0-120km), Tech. rep., AFGL-TR-86-0110, Environemental Research papers No. 954, 1986.

Ansmann, A., Petzold, A., Kandler, K., Tegen, I., Wendisch, M., Müller, D., Weinzierl, B., Müller, T., and Heintzenberg, J.: Saharan Mineral Dust Experiments SAMUM-1 and SAMUM-2: What have we learned?, Tellus B, 63, 403–429, doi:10.1111/j.1600-0889.2011.00555.x, 2011.

Ben-Ami, Y., Koren, I., and Altaratz, O.: Patterns of North African dust transport over the Atlantic: winter vs. summer, based on CALIPSO first year data, Atmos. Chem. Phys., 9, 7867–7875, doi:10.5194/acp-9-7867-2009, 2009.

Bissonnette, L. R., Bruscaglioni, P., Ismaelli, A., Zaccanti, G., Cohen, A., Benayahu, Y., Kleiman, M., Egert, S., Flesia, C., Schwendimann, P., Starkov, A. V., Noormohammadian, M., Oppel, U. G., Winker, D. M., Zege, E. P., Katsev, I. L., and Polonsky, I. N.: LIDAR multiple scattering from clouds, Appl. Phys. B, 60, 355–362, doi:10.1007/BF01082271, 1995.

Carlson, T. N. and Prospero, J. M.: The large-scale movement of Saharan air outbreaks over the northern equatorial Atlantic, J. Appl. Meteor., 11, 283–297, doi:10.1175/1520-0450(1972)011<0283:TLSMOS>2.0.CO;2, 1972.

Chen, S.-H., Wang, S.-H., and Waylonis, M.: Modification of Saharan air layer and environmental shear over the eastern Atlantic Ocean by dust-radiation effects, J. Geophys. Res. Atmos., 115, D21 202, doi:10.1029/2010JD014158, 2010.

Clift, R., Grace, J. R., and Weber, M. E.: Bubbles, Drops, and Particles, Academic Press, 1978.

Cuesta, J., Marsham, J. H., Parker, D. J., and Flamant, C.: Dynamical mechanisms controlling the vertical redistribution of dust and the thermodynamic structure of the West Saharan atmospheric boundary layer during summer, Atmosph. Sci. Lett., 10, 34–42, doi:10.1002/asl.207, 2009.

Denjean, C., Cassola, F., Mazzino, A., Triquet, S., Chevaillier, S., Grand, N., Bourrianne, T., Momboisse, G., Sellegri, K., Schwarzenbock, A., Freney, E., Mallet, M., and Formenti, P.: Size distribution and optical properties of mineral dust aerosols transported in the western Mediterranean, Atmos. Chem. Phys., 16, 1081–1104, doi:10.5194/acp-16-1081-2016, 2016a.

Denjean, C., Formenti, P., Desboeufs, K., Chevaillier, S., Triquet, S., Maillé, M., Cazaunau, M., Laurent, B., Mayol-Bracero, O. L., Vallejo, P., Quiñones, M., Gutierrez-Molina, I. E., Cassola, F., Prati, P., Andrews, E., and Ogren, J.: Size distribution and optical properties of African mineral dust after intercontinental transport, J. Geophys. Res. Atmos., 121, 7117–7138, doi:10.1002/2016JD024783, 2016b.

Draxler, R. and Rolph, G.: HYSPLIT (HYbrid Single-Particle Lagrangian Integrated Trajectory) Model access via NOAA ARL READY Website (http://ready.arl.noaa.gov/HYSPLIT.php), NOAA Air Resources Laboratory, Silver Spring, MD, 2015.

Esselborn, M., Wirth, M., Fix, A., Weinzierl, B., Rasp, K., Tesche, M., and Petzold, A.: Spatial distribution and optical properties of Saharan dust observed by airborne high spectral resolution lidar during SAMUM 2006, Tellus B, 61, 131–143, doi:10.1111/j.1600-0889.2008.00394.x, 2009.

Freudenthaler, V., Seefeldner, M., Groß, S., and Wandinger, U.: Accuracy of linear depolarization ratios in clean air ranges measured with POLIS-6 at 355 and 532 nm, EPJ Web of Conferences, 119, 25 013, doi:10.1051/epjconf/201611925013, 2016.

Gasteiger, J., Wiegner, M., Groß, S., Freudenthaler, V., Toledano, C., Tesche, M., and Kandler, K.: Modeling lidar-relevant optical properties of complex mineral dust aerosols, Tellus B, 63, 725–741, doi:10.1111/j.1600-0889.2011.00559.x, 2011.

Ginoux, P.: Effects of nonsphericity on mineral dust modeling, J. Geophys. Res. Atmos., 108, 4052, doi:10.1029/2002JD002516, 2003.

Groß, S., Freudenthaler, V., Schepanski, K., Toledano, C., Schäfler, A., Ansmann, A., and Weinzierl, B.: Optical properties of long-range transported Saharan dust over Barbados as measured by dual-wavelength depolarization Raman lidar measurements, Atmos. Chem. Phys., 15, 11 067–11 080, doi:10.5194/acp-15-11067-2015, 2015.

Haarig, M., Althausen, D., Ansmann, A., Klepel, A., Baars, H., Engelmann, R., Groß, S., and Freudenthaler, V.: Measurement of the Linear Depolarization Ratio of Aged Dust at Three Wavelengths (355, 532 and 1064 nm) Simultaneously over Barbados, EPJ Web of Conferences, 119, 18 009, doi:10.1051/epjconf/201611918009, 2016.

Heintzenberg, J.: The SAMUM-1 experiment over Southern Morocco: overview and introduction, Tellus B, 61, 2–11, doi:10.1111/j.1600-0889.2008.00403.x, 2009.

Hess, M., Koepke, P., and Schult, I.: Optical Properties of Aerosols and Clouds: The Software Package OPAC, Bull. Amer. Meteor. Soc., 79, 831–844, doi:10.1175/1520-0477(1998)079<0831:OPOAAC>2.0.CO;2, 1998.

Hinds, W. C.: Aerosol technology: properties, behavior, and measurement of airborne particles, John Wiley & Sons, 1999.

Hunt, W. H., Winker, D. M., Vaughan, M. A., Powell, K. A., Lucker, P. L., and Weimer, C.: CALIPSO Lidar Description and Performance Assessment, J. Atmos. Oceanic Technol., 26, 1214–1228, doi:10.1175/2009JTECHA1223.1, 2009.

Järvinen, E., Kemppinen, O., Nousiainen, T., Kociok, T., Möhler, O., Leisner, T., and Schnaiter, M.: Laboratory investigations of mineral dust near-backscattering depolarization ratios, J. Quant. Spectrosc. Radiat. Transf., 178, 192–208, doi:10.1016/j.jqsrt.2016.02.003, 2016.

Kaaden, N., Massling, A., Schladitz, A., Müller, T., Kandler, K., Schütz, L., Weinzierl, B., Petzold, A., Tesche, M., Leinert, S., Deutscher, C., Ebert, M., Weinbruch, S., and Wiedensohler, A.: State of mixing, shape factor, number size distribution, and hygroscopic growth of the Saharan anthropogenic and mineral dust aerosol at Tinfou, Morocco, Tellus B, 61, 51–63, doi:10.1111/j.1600-0889.2008.00388.x, 2009.

Kandler, K., Lieke, K., Benker, N., Emmel, C., Küpper, M., Müller-Ebert, D., Scheuvens, D., Schladitz, A., Schütz, L., and Weinbruch, S.: Electron microscopy of particles collected at Praia, Cape Verde, during the Saharan Mineral dust experiment: particle chemistry, shape, mixing state and complex refractive index, Tellus B, 63, 475–496, doi:10.1111/j.1600-0889.2011.00550.x, 2011.

Knippertz, P., Ansmann, A., Althausen, D., Müller, D., Tesche, M., Bierwirth, E., Dinter, T., Müller, T., Von Hoyningen-Huene, W., Schepanski, K., Wendisch, M., Heinold, B., Kandler, K., Petzold, A., Schütz, L., and Tegen, I.: Dust mobilization and transport in the northern Sahara during SAMUM 2006 - a meteorological overview, Tellus B, 61, 12–31, doi:10.1111/j.1600-0889.2008.00380.x, 2009.

Koepke, P., Gasteiger, J., and Hess, M.: Technical Note: Optical properties of desert aerosol with non-spherical mineral particles: data incorporated to OPAC, Atmos. Chem. Phys., 15, 5947–5956, doi:10.5194/acp-15-5947-2015, 2015.

Liu, Z., Omar, A., Vaughan, M., Hair, J., Kittaka, C., Hu, Y., Powell, K., Trepte, C., Winker, D., Hostetler, C., Ferrare, R., and Pierce, R.: CALIPSO lidar observations of the optical properties of Saharan dust: A case study of long-range transport, J. Geophys. Res., 113, D07 207, doi:10.1029/2007JD008878, 2008.

Liu, Z., Vaughan, M., Winker, D., Kittaka, C., Getzewich, B., Kuehn, R., Omar, A., Powell, K., Trepte, C., and Hostetler, C.: The CALIPSO Lidar Cloud and Aerosol Discrimination: Version 2 Algorithm and Initial Assessment of Performance, J. Atmos. Oceanic Technol., 26, 1198–1213, doi:10.1175/2009JTECHA1229.1, 2009.

Liu, Z., Fairlie, T. D., Uno, I., Huang, J., Wu, D., Omar, A., Kar, J., Vaughan, M., Rogers, R., Winker, D., Trepte, C., Hu, Y., Sun, W., Lin, B., and Cheng, A.: Transpacific transport and evolution of the optical properties of Asian dust, J. Quant. Spectrosc. Radiat. Transf., 116, 24–33, doi:10.1016/j.jqsrt.2012.11.011, 2013.

Loth, E.: Drag of non-spherical solid particles of regular and irregular shape, Powder Technol., 182, 342–353, doi:10.1016/j.powtec.2007.06.001, 2008.

Mahowald, N., Albani, S., Kok, J. F., Engelstaeder, S., Scanza, R., Ward, D. S., and Flanner, M. G.: The size distribution of desert dust aerosols and its impact on the Earth system, Aeolian Res., 15, 53–71, doi:10.1016/j.aeolia.2013.09.002, 2014.

5 Maring, H., Savoie, D. L., Izaguirre, M. A., Custals, L., and Reid, J. S.: Mineral dust aerosol size distribution change during atmospheric transport, J. Geophys. Res. Atmos., 108, 8592, doi:10.1029/2002JD002536, 2003.

Mattis, I., Ansmann, A., Müller, D., Wandinger, U., and Althausen, D.: Dual-wavelength Raman lidar observations of the extinction-to-backscatter ratio of Saharan dust, Geophys. Res. Lett., 29, 20–1–20–4, doi:10.1029/2002GL014721, 2002.

NASA: CALIPSO Lidar Level 2 Aerosol Profile Products Version 3.01, doi:10.5067/CALIOP/CALIPSO/CAL_LID_L2_05kmAPro-Prov-
10 V3-01_L2-003.01, 2010.

Otto, S., Bierwirth, E., Weinzierl, B., Kandler, K., Esselborn, M., Tesche, M., Schladitz, A., Wendisch, M., and Trautmann, T.: Solar radiative effects of a Saharan dust plume observed during SAMUM assuming spheroidal model particles, Tellus B, 61, 270–296, doi:10.1111/j.1600-0889.2008.00389.x, 2009.

Papayannis, A., Amiridis, V., Mona, L., Tsaknakis, G., Balis, D., Bösenberg, J., Chaikovski, A., de Tomasi, F., Grigorov, I., Mattis, I., Mitev,
15 V., Müller, D., Nickovic, S., Pérez, C., Pietruczuk, A., Pisani, G., Ravetta, F., Rizi, V., Sicard, M., Trickl, T., Wiegner, M., Gerding, M., Mamouri, R. E., D'Amico, G., and Pappalardo, G.: Systematic lidar observations of Saharan dust over Europe in the frame of EARLINET (2000–2002), J. Geophys. Res., 113, D10 204, doi:10.1029/2007JD009028, 2008.

Pappalardo, G., Amodeo, A., Apituley, A., Comeron, A., Freudenthaler, V., Linné, H., Ansmann, A., Bösenberg, J., D'Amico, G., Mattis, I., Mona, L., Wandinger, U., Amiridis, V., Alados-Arboledas, L., Nicolae, D., and Wiegner, M.: EARLINET: towards an advanced sustainable
20 European aerosol lidar network, Atmos. Meas. Tech., 7, 2389–2409, doi:10.5194/amt-7-2389-2014, 2014.

Powell, K. A., Hostetler, C. A., Vaughan, M. A., Lee, K.-P., Trepte, C. R., Rogers, R. R., Winker, D. M., Liu, Z., Kuehn, R. E., Hunt, W. H., and Young, S. A.: CALIPSO Lidar Calibration Algorithms. Part I: Nighttime 532-nm Parallel Channel and 532-nm Perpendicular Channel, J. Atmos. Oceanic Technol., 26, 2015–2033, doi:10.1175/2009JTECHA1242.1, 2009.

Prospero, J. M. and Carlson, T. N.: Vertical and areal distribution of Saharan dust over the western equatorial North Atlantic Ocean, J.
25 Geophys. Res, 77, 5255–5265, doi:10.1029/JC077i027p05255, 1972.

Reid, J. S., Kinney, J. E., Westphal, D. L., Holben, B. N., Welton, E. J., Tsay, S., Eleuterio, D. P., Campbell, J. R., Christopher, S. A., Colarco, P. R., Jonsson, H. H., Livingston, J. M., Maring, H. B., Meier, M. L., Pilewskie, P., Prospero, J. M., Reid, E. A., Remer, L. A., Russell, P. B., Savoie, D. L., Smirnov, A., and Tanré, D.: Analysis of measurements of Saharan dust by airborne and ground-based remote sensing methods during the Puerto Rico Dust Experiment (PRIDE), J. Geophys. Res. Atmos., 108, 8586, doi:10.1029/2002JD002493, 2003.

30 Ryder, C. L., Highwood, E. J., Rosenberg, P. D., Trembath, J., Brooke, J. K., Bart, M., Dean, A., Crosier, J., Dorsey, J., Brindley, H., Banks, J., Marsham, J. H., McQuaid, J. B., Sodemann, H., and Washington, R.: Optical properties of Saharan dust aerosol and contribution from the coarse mode as measured during the Fennec 2011 aircraft campaign, Atmos. Chem. Phys., 13, 303–325, doi:10.5194/acp-13-303-2013, 2013.

Sakai, T., Nagai, T., Zaizen, Y., and Mano, Y.: Backscattering linear depolarization ratio measurements of mineral, sea-salt, and ammonium
35 sulfate particles simulated in a laboratory chamber, Appl. Opt., 49, 4441–4449, doi:10.1364/AO.49.004441, 2010.

Sassen, K.: The Polarization Lidar Technique for Cloud Research: A Review and Current Assessment, Bull. Amer. Meteor. Soc., 72, 1848–1866, doi:10.1175/1520-0477(1991)072<1848:TPLTFC>2.0.CO;2, 1991.

Schütz, L.: Long range transport of desert dust with special emphasis on the Sahara, Ann. N. Y. Acad. Sci., 338, 515–532, doi:10.1111/j.1749-6632.1980.tb17144.x, 1980.

Tsamalis, C., Chédin, A., Pelon, J., and Capelle, V.: The seasonal vertical distribution of the Saharan Air Layer and its modulation by the wind, Atmos. Chem. Phys., 13, 11 235–11 257, doi:10.5194/acp-13-11235-2013, 2013.

Ulanowski, Z., Bailey, J., Lucas, P. W., Hough, J. H., and Hirst, E.: Alignment of atmospheric mineral dust due to electric field, Atmos. Chem. Phys., 7, 6161–6173, doi:10.5194/acp-7-6161-2007, 2007.

van der Does, M., Korte, L. F., Munday, C. I., Brummer, G.-J. A., and Stuut, J.-B. W.: Particle size traces modern Saharan dust transport and deposition across the equatorial North Atlantic, Atmos. Chem. Phys., 16, 13 697–13 710, doi:10.5194/acp-16-13697-2016, 2016.

Vaughan, M. A., Powell, K. A., Kuehn, R. E., Young, S. A., Winker, D. M., Hostetler, C. A., Hunt, W. H., Liu, Z., McGill, M. J., and Getzewich, B. J.: Fully Automated Detection of Cloud and Aerosol Layers in the CALIPSO Lidar Measurements, J. Atmos. Oceanic Technol., 26, 2034–2050, doi:10.1175/2009JTECHA1228.1, 2009.

Wandinger, U., Tesche, M., Seifert, P., Ansmann, A., Müller, D., and Althausen, D.: Size matters: Influence of multiple scattering on CALIPSO light-extinction profiling in desert dust, Geophys. Res. Lett., 37, L10 801, doi:10.1029/2010GL042815, 2010.

Weinzierl, B., Petzold, A., Esselborn, M., Wirth, M., Rasp, K., Kandler, K., Schütz, L., Koepke, P., and Fiebig, M.: Airborne measure-ments of dust layer properties, particle size distribution and mixing state of Saharan dust during SAMUM 2006, Tellus B, 61, 96–117, doi:10.1111/j.1600-0889.2008.00392.x, 2009.

Weinzierl, B., Sauer, D., Esselborn, M., Petzold, A., Veira, A., Rose, M., Mund, S., Wirth, M., Ansmann, A., Tesche, M., Groß, S., and Freudenthaler, V.: Microphysical and optical properties of dust and tropical biomass burning aerosol layers in the Cape Verde region - An overview of the airborne in situ and lidar measurements during SAMUM-2, Tellus B, 63, 589–618, doi:10.1111/j.1600-0889.2011.00566.x, 2011.

Weinzierl, B., Ansmann, A., Prospero, J. M., Althausen, D., Benker, N., Chouza, F., Dollner, M., Farrell, D., Fomba, W. K., Freudenthaler, V., Gasteiger, J., Groß, S., Haarig, M., Heinold, B., Kandler, K., Kristensen, T. B., Mayol-Bracero, O. L., Müller, T., Reitebuch, O., Sauer, D., Schäfler, A., Schepanski, K., Spanu, A., Tegen, I., Toledano, C., and Walser, A.: The Saharan Aerosol Long-range Transport and Aerosol-Cloud-Interaction Experiment (SALTRACE): overview and selected highlights, Bull. Amer. Meteor. Soc., doi:10.1175/BAMS-D-15-00142.1, 2017.

Wiegner, M., Groß, S., Freudenthaler, V., Schnell, F., and Gasteiger, J.: The May/June 2008 Saharan dust event over Munich: Intensive aerosol parameters from lidar measurements, J. Geophys. Res., 116, D23 213, doi:10.1029/2011JD016619, 2011.

Winker, D. M., Vaughan, M. A., Omar, A., Hu, Y., Powell, K. A., Liu, Z., Hunt, W. H., and Young, S. A.: Overview of the CALIPSO Mission and CALIOP Data Processing Algorithms, J. Atmos. Oceanic Technol., 26, 2310–2323, doi:10.1175/2009JTECHA1281.1, 2009.

Yang, W., Marshak, A., Kostinski, A. B., and Várnai, T.: Shape-induced gravitational sorting of Saharan dust during transatlantic voyage: Evidence from CALIOP lidar depolarization measurements, Geophys. Res. Lett., 40, 3281–3286, doi:10.1002/grl.50603, 2013.

Young, S. A.: Uncertainty Analysis for Particulate Backscatter, Extinction and Optical Depth Retrievals reported in the CALIPSO Level 2, Version 3 Data Release, https://eosweb.larc.nasa.gov/sites/default/files/project/calipso/CALIOP_Version3_Extinction_Error_Analysis.pdf, 2010.

Yurkin, M. A. and Hoekstra, A. G.: The discrete-dipole-approximation code ADDA: Capabilities and known limitations, J. Quant. Spectrosc. Radiat. Transf., 112, 2234–2247, doi:10.1016/j.jqsrt.2011.01.031, 2011.